Available online at www.sciencedirect.com
ScienceDirect
Journal of Computational Physics 222 (2007) 131–154
JOURNAL OF COMPUTATIONAL PHYSICS
www.elsevier.com/locate/jcp

Application of the GRP scheme to open channel flow equations

A. Birman [a], J. Falcovitz [b,*]

[a] Center for Mathematics and Its Applications, Australian National University, Canberra, ACT 0200, Australia
[b] Institute of Mathematics, The Hebrew University of Jerusalem, Jerusalem 91904, Israel

Received 18 November 2005; received in revised form 17 July 2006; accepted 17 July 2006
Available online 7 September 2006

Abstract

The GRP (generalized Riemann problem) scheme, originally conceived for gasdynamics, is reformulated for the numerical integration of the shallow water equations in channels of rectangular cross-section, variable width and bed profile, including a friction model for the fluid–channel shear stress. This scheme is a second-order analytic extension of the first-order Godunov-scheme, based on time-derivatives of flow variables at cell-interfaces resulting from piecewise-linear data reconstruction in cells. The second-order time-integration is based on solutions to generalized Riemann problems at cell-interfaces, thus accounting for the full governing equations, including source terms. The source term due to variable bed elevation is treated in a well-balanced way so that quiescent flow is exactly replicated; this is done by adopting the Surface Gradient Method (SGM). Several problems of steady or unsteady open channel flow are considered, including the terms corresponding to variable channel width and bed elevation, as well as to shear stress at the fluid–channel interface (using the Manning friction model). In all these examples remarkable agreement is obtained between the numerical integration and the exact or accurate solutions.

Keywords: Shallow water; Quasi-1D flow; Generalized Riemann problem (GRP); Hyperbolic conservation laws; Second-order scheme; Hydraulic jump; Open channel

1. Introduction

Efficient and accurate mathematical simulations to the physically significant phenomena in a given flow scenario are essential to modern hydraulic engineering. Of particular interest are flows in open channels of varying width with bottom topography and shear stress at the fluid–channel interface. Since a detailed description of such flows by the equations of fluid mechanics is much too difficult, it is common practice to resort to the Saint Venant shallow water approximation for their modeling. The one-dimensional system that models such flows in channels of rectangular cross-section can be written as

* Corresponding author. Tel.: +972 2 6584176; fax: +972 2 5630702.
E-mail address: ccjf@math.huji.ac.il (J. Falcovitz).

0021-9991/$ - see front matter © 2006 Elsevier Inc. All rights reserved.
doi:10.1016/j.jcp.2006.07.008

$$\frac{\partial}{\partial t}[b(x)\mathbf{U}] + \frac{\partial}{\partial x}[b(x)\mathbf{F}(\mathbf{U})] + b(x)\frac{\partial}{\partial x}[\mathbf{G}(\mathbf{U})] + b(x)\mathbf{H}(\mathbf{U}) = 0, \tag{1.1}$$

$$\mathbf{U}(x,t) = \begin{bmatrix} h \\ hu \end{bmatrix}, \quad \mathbf{F}(\mathbf{U}) = \begin{bmatrix} uh \\ u^2 h \end{bmatrix}, \quad \mathbf{G}(\mathbf{U}) = \begin{bmatrix} 0 \\ \frac{gh^2}{2} \end{bmatrix},$$

$$\mathbf{H}(\mathbf{U}) = \begin{bmatrix} 0 \\ -gh(S_0 - S_f) \end{bmatrix}.$$

The notation for Eq. (1.1) is the following: (x,t) are the coordinate along the channel and the time; $h(x,t)$ is the water depth; $u(x,t)$ is the velocity; $b(x)$ is the channel width; $g = 9.81$ [m/s^2] is the gravity acceleration; $S_0 = -Z'(x)$ is the bed slope, with $Z(x)$ being the upward-pointing bed elevation. The flux function is split into a conservative term $\mathbf{F}$ and a non-conservative term $\mathbf{G}$. Finally, $\mathbf{H}$ is a source term combining the effects of gravity and friction. According to a tradition in hydraulics, the friction term S_f that models the shear stress at the channel–fluid interface is written in the form of a virtual bed slope (the consideration of a particular S_f function is deferred to example 5.5).

For the numerical integration of (1.1) we propose the GRP scheme, originally developed for fluid dynamics, which has been demonstrated to produce high-resolution simulations of shock wave phenomena (see [3] and references therein). This Godunov-type scheme uses the van Leer [15] piecewise-linear reconstruction in cells to evaluate mid-point fluxes from analytic solutions to generalized Riemann problems (GRP) at cell-interfaces. The resulting scheme constitutes a second-order extension of the (first-order) Godunov method, where all spatial derivatives in the PDE are approximated by upwind differencing. Thus, the effect of variable channel width is accounted for under the GRP discretization of the quasi-one-dimensional system (1.1), without requiring special treatment of the source terms proportional to $b'(x)$, as for example, in [8] or [16]. Another important feature of the GRP treatment of source terms concerns the evaluation of fluxes, as well as their time-derivatives, at cell-interfaces. Here the homogeneous part of the governing equations is taken as that of frictionless flow in a flat-bedded, constant-width channel. Consequently, the effects of variable channel geometry and stress at channel walls are fully accounted for in the second-order component of the time-integration under the GRP conservation law scheme.

Numerical solution of the shallow water system with variable bottom topography raises the issue of maintaining equilibrium in a state of quiescent flow. A centered-differencing of the bottom topography source term, however, replicates the state of quiescent flow only to within a truncation error. The key idea for eliminating this error, originally suggested by Bermúdez and Vázquez [4], is to employ an upwind differencing of the gravity source term, resulting in "source term – flux gradient balancing". Vázquez-Cendón [16] later proposed an upwind discretization of the gravity source term employing the Q-scheme of van Leer and Roe for the homogeneous part. LeVeque has proposed a scheme which balances the flux and bed slope terms, particularly for quasi-steady problems. Zhou et al. [17] have taken these ideas one step further by introducing the SGM (Surface Gradient Method) scheme that exactly replicates a quiescent state of the fluid in one or two space dimensions, naming this capability the "Z-property". The key idea is a data reconstruction expressing the water depth as $h(x,t) = \zeta(x,t) - Z(x)$, where $\zeta(x,t)$ is the water surface level. The SGM data reconstruction is readily adapted to a Godunov-type scheme such as the one proposed here, and we have incorporated it in a way that maintains the Z-property for both the first-order and the second-order terms of the GRP time integration.

GRP is a second-order accurate scheme based on solving generalized Riemann problems at cell-interfaces, with data comprising linearly distributed states on either side. This IVP is solved analytically for the full system (1.1), producing the fluxes and their time-derivatives at cell-interfaces. Thus, GRP is unique in that the effects of the governing PDE (including source terms) are accounted for in both the first-order and the second-order terms of the finite-difference integration. Our present GRP scheme for the shallow water system, being an adaptation of the original fluid dynamical version [3], relies on a transformation to Lagrange coordinates for the sake of the GRP analysis. Recently, a direct-Eulerian GRP version for the shallow water equations with bottom topography, which also possesses the previously mentioned Z-property, was proposed by Li and Chen [13]. This version, unlike the present one, does not include the features of variable channel width and friction model for shear stress at the channel–fluid interface, which have been included in formulating the generalized Riemann problems in the present GRP scheme.

The plan of the paper is as follows. In Section 2 we introduce the GRP finite-difference framework. In Section 3 we present the GRP analysis for centered rarefaction waves (CRW) and shock waves that arise in the solution to the (associated) Riemann problem at each cell-boundary point. This analysis leads to the solution of the point-centered generalized Riemann problems in Lagrangian and Eulerian coordinates. In Section 4 we present the implementation of the GRP analysis in an algorithmic way, by following the steps performed in a single time-integration cycle. In particular, we specify the scheme modifications introduced to achieve the aforementioned Z-property. In Section 5 we apply the GRP scheme to five examples, both steady and unsteady, having diverse source terms. In all these examples the numerical results compare favorably with the exact (or accurate) solutions, demonstrating that the GRP scheme replicates flow features such as shock or rarefaction waves with high level of accuracy and resolution. We conclude by summarizing in Section 6 the performance and novel aspects of our scheme. Finally, a proof of our scheme compliance with the Z-property is given in Appendix A.

2. The GRP finite-difference scheme

The GRP (generalized Riemann problem) method has been originally developed for the fluid dynamical equations, as a second-order analytic extension [1] of the (first-order) Godunov method. It possesses high-resolution shock-capturing capabilities, as has been demonstrated by numerous applications to the simulation of diverse shock wave phenomena ([3], and references therein).

A Godunov-type scheme for numerical integration of the shallow water system (1.1) is formulated as follows. The (x,t) computation domain is divided into a uniform grid of increments $(\Delta x, \Delta t)$. Cell i is the interval $\left[x_{i-\frac{1}{2}}, x_{i+\frac{1}{2}}\right]$ where $x_{i-\frac{1}{2}} = x_o + (i-1/2)\Delta x$ and x_o is an arbitrary constant. The time coordinate is discretized as $t_n = n\Delta t$ with $n = 0, 1, 2, \ldots$, where Δt is the integration time step. Let $\mathbf{U}_i^n$ denote the finite-difference approximation to the average value of $\mathbf{U}(x,t)$ over cell i at time t_n. Similarly, let $\mathbf{U}_{i+\frac{1}{2}}^{n+\frac{1}{2}}$ denote the finite-difference approximation of $\mathbf{U}(x,t)$ at cell-interface $x_{i+\frac{1}{2}}$, averaged over the time interval $[t_n, t_{n+1}]$. Following the approach proposed by Godunov [9], a conservation law scheme for system (1.1) can be written as

$$\begin{aligned}
\mathbf{U}_i^{n+1} &= \mathbf{U}_i^n - \frac{\Delta t}{\Delta s_i}\left[b(x_{i+\frac{1}{2}})\mathbf{F}(\mathbf{U})_{i+\frac{1}{2}}^{n+\frac{1}{2}} - b(x_{i-\frac{1}{2}})\mathbf{F}(\mathbf{U})_{i-\frac{1}{2}}^{n+\frac{1}{2}}\right] \\
&\quad - \frac{\Delta t}{\Delta x}\left[\mathbf{G}(\mathbf{U})_{i+\frac{1}{2}}^{n+\frac{1}{2}} - \mathbf{G}(\mathbf{U})_{i-\frac{1}{2}}^{n+\frac{1}{2}}\right] - \Delta t\mathbf{H}(\mathbf{U}_i^{n+\frac{1}{2}}), \quad \text{where} \\
\Delta s_i &= \int_{x_{i-\frac{1}{2}}}^{x_{i+\frac{1}{2}}} b(x)\,\mathrm{d}x.
\end{aligned} \tag{2.1}$$

The specific nature of the finite-difference approximation (2.1) is largely decided by the choice of algorithms for the time-centered source values $\mathbf{H}(\mathbf{U}_i^{n+\frac{1}{2}})$ at cell-centers, and for the time-centered values $\mathbf{U}_{i+\frac{1}{2}}^{n+\frac{1}{2}}$ at cell-interfaces, on which the numerical fluxes $\mathbf{F}$, $\mathbf{G}$ depend.

While $\mathbf{U}_i^{n+\frac{1}{2}}$ may be evaluated implicitly as $\frac{1}{2}(\mathbf{U}_i^n + \mathbf{U}_i^{n+1})$, an appropriate interpretation to a time-centered cell-interface value $\mathbf{U}_{i+\frac{1}{2}}^{n+\frac{1}{2}}$ is not immediate. The key idea of the GRP method is to evaluate such terms *analytically* from their time-derivatives

$$\begin{aligned}
\mathbf{U}_{i+\frac{1}{2}}^{n+\frac{1}{2}} &= \mathbf{U}_{i+\frac{1}{2}}^n + \frac{\Delta t}{2}\left[\frac{\partial}{\partial t}\mathbf{U}\right]_{i+\frac{1}{2}}^n, \\
\mathbf{F}(\mathbf{U})_{i+\frac{1}{2}}^{n+\frac{1}{2}} &= \mathbf{F}\left(\mathbf{U}_{i+\frac{1}{2}}^{n+\frac{1}{2}}\right), \\
\mathbf{G}(\mathbf{U})_{i+\frac{1}{2}}^{n+\frac{1}{2}} &= \mathbf{G}\left(\mathbf{U}_{i+\frac{1}{2}}^{n+\frac{1}{2}}\right).
\end{aligned} \tag{2.2}$$

The term $\mathbf{U}_{i+1/2}^n$ and its time-derivative in (2.2) are obtained by solving at each cell-interface an IVP (initial value problem) for (1.1) with the data approximated as piecewise-linear in cells and discontinuous at cell-interfaces. This idea was originally proposed by van Leer [15], leading to the fluid dynamical MUSCL method. Roughly speaking, $\mathbf{U}_{i+1/2}^n$ is obtained by solving an "associated Riemann problem" corresponding to the data jump at cell-interface points, while the respective time-derivative is obtained by taking into account the slopes

of data on either side of the cell-interface points, as well as all source terms in the governing equations. The full analytic treatment of this extended IVP, referred to as a "generalized Riemann problem" [1,2], yields expressions for the time-derivatives in (2.2) which for a γ-law gas are given in terms of elementary functions. Based on the well-known analogy between the shallow water and the fluid dynamical equations for isentropic flow of a $\gamma = 2$ ideal gas [6,11], the GRP scheme for shallow water may readily be obtained from the γ-law gasdynamical GRP (with a modified "isentropic shock" jump condition for the shallow water shock wave).

For the fluid dynamical system of three equations the solution to a Riemann problem consists of three waves: a left-propagating wave, a right-propagating wave, and a contact discontinuity separating the two waves. Each wave is either a shock or a centered rarefaction. The 1D shallow water system (1.1) consists of two equations and hence has a two-wave Riemann solution: a left-propagating wave and a right-propagating wave, each one being either a shock (hydraulic jump) or a centered rarefaction. Therefore, the GRP for shallow water may be formulated directly in Eulerian coordinates, rather than in the Lagrange framework as in the original GRP method. Indeed, this Eulerian approach was recently proposed by Li and Chen [13], who used Riemann invariants in the GRP analysis of shallow water equations with bottom topography, but without variable width and friction. However, we propose to retain the Lagrange formulation for the shallow water GRP, albeit the absence of a contact discontinuity in the Riemann solution. The analytic complexities of the two approaches are not markedly different, while the Lagrange formulation has the potential advantage of natural extension to ALE (arbitrary Lagrange Euler) grid [10]. Such capability might be used, for example, to compute a piston-driven channel flow, where the piston is presented by a moving Lagrangian point.

The gravitational source term $\mathbf{H}$ in (1.1) raises an issue of "source term–flux gradient balancing" as pointed out by Bermúdez and Vázquez [4]. The imbalance appears as truncation error in the case of an initial quiescent flow state with varying bed elevation, since $h(x,\ 0)$ is not uniform in that case. Following Zhou et al. [17] we introduce the surface level variable $\zeta(z,t) = h(x,t) + Z(x)$, and incorporate the Surface Gradient Method (SGM) [17] into the shallow water GRP scheme, so that quiescent flow is exactly replicated (i.e., the resulting scheme possesses the Z-property, as it was named in [17]). This modification was also incorporated into the direct-Eulerian GRP scheme of Li and Chen [13].

3. The GRP analysis

The extension of the finite-difference scheme (2.1) to second-order accuracy is based on solutions to generalized Riemann problems (GRP) at cell-interfaces. The required analysis is conducted in (local) Lagrange coordinates, then transformed back to the Eulerian framework (in which the governing equation and finite-difference approximation are formulated). Here we present, step by step, the necessary concepts and analytic results, concluding with the expressions needed for evaluating the time-centered fluxes (2.2).

3.1. Governing equations in lagrange coordinates

Since the GRP analysis is conducted in Lagrange coordinates, we start by transforming the shallow water system (1.1) into the Lagrangian framework. Let the Lagrange coordinate ξ be given by the differential relation

$$\mathrm{d}\xi = b(x)h(x,t)\,\mathrm{d}x, \quad \xi(0) = 0. \tag{3.1}$$

The Lagrangian time-derivative of a flow variable $Q(\xi,t) = Q(x,t)$ is then given by

$$\frac{\partial}{\partial t}Q(\xi,t) = \frac{\partial}{\partial t}Q(x,t)\bigg|_{x=x(\xi,t)} + u(\xi,t)\frac{\partial}{\partial x}Q(x,t)\bigg|_{x=x(\xi,t)}, \tag{3.2}$$

where $x(\xi,t)$ is determined by the differential relation (3.1). The system (1.1) is then written in Lagrange coordinates as

$$\begin{aligned}&\frac{\partial\tau}{\partial t}-\frac{\partial}{\partial\xi}(bu)=0,\\&\frac{\partial u}{\partial t}+\frac{\partial}{\partial\xi}\left(\frac{bg}{2\tau^2}\right)-\lambda\frac{g}{2\tau}-g(S_0-S_f)=0,\end{aligned}\tag{3.3}$$

where $\tau(\xi,t)=\frac{1}{h}(\xi,t)$, and $\partial b/\partial\xi$ is given by

$$\frac{\partial b}{\partial\xi}=\frac{1}{bh}\frac{\partial b}{\partial x}=\frac{1}{h}\frac{b'}{b}=\frac{\lambda}{h},\quad \lambda=\frac{b'(x)}{b(x)}.\tag{3.4}$$

The homogeneous part of (3.3) can be written as

$$\frac{\partial\mathbf{V}}{\partial t}+\frac{\partial\mathbf{L}}{\partial\xi}=\mathbf{0},\tag{3.5}$$

where $\mathbf{V}(\xi,t)=[\tau(\xi,t),u(\xi,t)]^{\mathrm{T}}$, $\mathbf{L}(\mathbf{V})=[-bu,bg/2\tau^2]^{\mathrm{T}}$.

The hyperbolic system (3.3) leads to the following differential relations along the *characteristic lines* $C_\pm$

$$c^2\mathrm{d}h\pm\kappa\mathrm{d}u+[u\kappa\lambda c\mp c^3(S_0-S_f)]\mathrm{d}t=0,\quad \text{along } C_\pm:\ \frac{\mathrm{d}\xi}{\mathrm{d}t}=\pm b\kappa,\tag{3.6}$$

where $c=\sqrt{gh}$ is the shallow water wave speed and $\kappa=hc$ is the respective Lagrangian speed.

3.2. The Riemann problem (RP)

The Riemann problem is an IVP for the homogeneous system (3.5) that plays a central role in the analysis. The data for an RP consists of any two uniform states $\mathbf{V}(\xi,0)=\mathbf{V}_\mathrm{L}$ for $\xi<0$, $\mathbf{V}(\xi,0)=\mathbf{V}_\mathrm{R}$ for $\xi>0$, separated by a discontinuity at $\xi=0$ (Fig. 1a). The solution to this IVP is self-similar, i.e., it depends on ξ/t rather than on the two variables (ξ,t), and is denoted as $\mathbf{V}(\xi,t)=\mathbf{R}(\xi/t;\mathbf{V}_\mathrm{L},\mathbf{V}_\mathrm{R})$. It is constructed in terms of two "elementary waves" as building blocks: a centered rarefaction wave (CRW) and a shock wave. Each wave corresponds to a point on an "interaction curve", which is a relation $u=u(h;h_0,u_0)$ between the post-wave values u,h, given the pre-wave state (h_0,u_0), with the sign $\pm$ denoting propagation in the $\pm\xi$ direction. The interaction curves are composed of two branches: a CRW branch with $h<h_0$ and a shock branch with $h>h_0$.

Integrating the homogeneous differential relations (3.6) along a $C_\pm$ characteristic curve yields (at $t\to 0+$) the following expression for the CRW branch

$$u(h)=u_0\pm 2\sqrt{g}(h^{1/2}-h_0^{1/2}),\quad (h<h_0).\tag{3.7}$$

The shock interaction branch is obtained by considering the jump condition for (3.5), which is written as

$$\begin{aligned}&\tilde{S}(\tau-\tau_0)=-(u-u_0)b,\\&\tilde{S}(u-u_0)=b\frac{g}{2}(\tau^{-1}-\tau_0^{-1})(\tau^{-1}+\tau_0^{-1}),\end{aligned}$$

with $\tilde{S}$ representing the (Lagrange) velocity of shock propagation. From these equations we get for the shock velocity

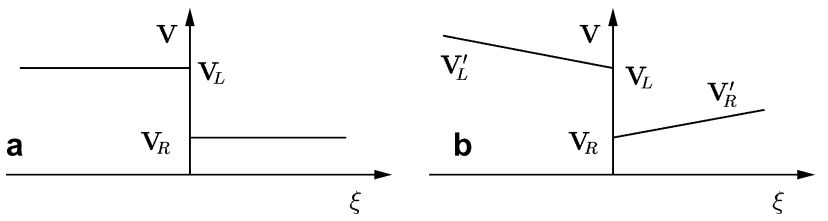

Fig. 1. Initial data: (a) Riemann problem, (b) generalized Riemann problem.

$$\tilde{S} = \left(\frac{\mathrm{d}\xi}{\mathrm{d}t}\right)_{\text{shock}} = \pm b\sqrt{\frac{g}{2}hh_0(h+h_0)} = \sigma(h,h_0) \tag{3.8}$$

and for the shock branch of the interaction curve

$$u(h) = u_0 \pm \Phi(h,h_0), \quad \Phi(h,h_0) = (h-h_0)\sqrt{\frac{g}{2}\left(\frac{1}{h_0}+\frac{1}{h}\right)}, \quad (h > h_0). \tag{3.9}$$

Note that while the Lagrangian shock velocity (3.8) depends on $b(x)$, the shock interaction curve (i.e., the *jump condition*) is independent of $b(x)$. Moreover, the interaction curves are independent of the coordinate system, and could have been derived from the Eulerian-frame system (1.1).

The solution to an RP is constructed by seeking two "elementary waves" separated by a mid-state $\mathbf{V}^* = [h^*, u^*]$ lying on both interaction curves:

$$u^* = u(h^*;\mathbf{V}_\mathrm{L}) = u(h^*;\mathbf{V}_\mathrm{R}). \tag{3.10}$$

The type of wave on either side is determined by whether the intersection point lies on a shock or a CRW branch.

3.3. The generalized Riemann problem (GRP)

Of special interest to us is the GRP which is the IVP for (3.3) subject to the following initial data:

$$\mathbf{V}(\xi,0) = \begin{cases} \mathbf{V}_\mathrm{L} + \xi\mathbf{V}'_\mathrm{L}, & \xi < 0, \\ \mathbf{V}_\mathrm{R} + \xi\mathbf{V}'_\mathrm{R}, & \xi > 0, \end{cases} \tag{3.11}$$

where $\mathbf{V}_\mathrm{L}$, $\mathbf{V}_\mathrm{R}$ define the initial discontinuity, and $\mathbf{V}'_\mathrm{L}, \mathbf{V}'_\mathrm{R}$ are the slopes on either side (see Fig. 1b).

The first stage of solving a GRP at cell-interfaces is the solution to the associated Riemann problem, namely the RP obtained by setting $\mathbf{V}'_\mathrm{L} = \mathbf{V}'_\mathrm{R} = 0$. We denote this (self-similar) solution by $\mathbf{V}^A(\xi,t) = \mathbf{R}^A(\theta;\mathbf{V}_\mathrm{L},\mathbf{V}_\mathrm{R})$, where $\theta = \xi/t$.

The basic assumption of the GRP analysis [3] is that the solution $\mathbf{V}(\xi,t)$ to the GRP at $t \to 0+$ and $\xi = \theta t$ coincides with $\mathbf{R}^A(\theta;\mathbf{V}_\mathrm{L},\mathbf{V}_\mathrm{R})$. At $t > 0$ $\mathbf{V}(\xi,t)$ evolves in a non-self-similar way, due to the slopes $\mathbf{V}'_\mathrm{L}$, $\mathbf{V}'_\mathrm{R}$ in the initial data (3.11), as well as to the source terms in (3.3).

The GRP solution we seek is the time-derivative $\partial\mathbf{V}(\xi,t)/\partial t$ at $\xi = 0$ and $t \to 0+$. Or equivalently, the time-derivatives of the mid-state $u^*(t)$, $h^*(t)$ at $t \to 0+$, noting that in the GRP solution, unlike the self-similar RP solution of (3.5), the mid-state evolves in time (see the schematic wave diagram in Fig. 2b for the GRP whose associated RP solution is depicted in Fig. 2a).

The main result of the GRP analysis is that the time-derivatives $\left(\frac{\partial h}{\partial t}\right)^*$, $\left(\frac{\partial u}{\partial t}\right)^*$ are related by a pair of linear equations

$$\begin{aligned} a_\mathrm{L}\left(\frac{\partial u}{\partial t}\right)^* + b_\mathrm{L}\left(\frac{\partial h}{\partial t}\right)^* &= d_\mathrm{L}, \\ a_\mathrm{R}\left(\frac{\partial u}{\partial t}\right)^* + b_\mathrm{R}\left(\frac{\partial h}{\partial t}\right)^* &= d_\mathrm{R}, \end{aligned} \tag{3.12}$$

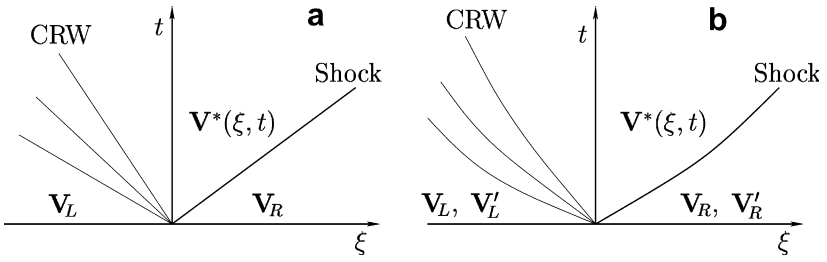

Fig. 2. Solution to: (a) Riemann problem, (b) generalized Riemann problem.

where a_L, b_L, d_L depend solely on $\mathbf{V}^*, \mathbf{V}_L, \mathbf{V}'_L, \lambda, S_0, S_f$, and likewise a_R, b_R, d_R depend solely on $\mathbf{V}^*, \mathbf{V}_R, \mathbf{V}'_R, \lambda, S_0, S_f$. In the following sections we consider the GRP analysis for the two cases of shock wave and CRW. To fix ideas, we assume that the left wave is a CRW and the right wave is a shock, and we first consider the GRP analysis of the latter.

3.4. GRP analysis of a shock wave

Consider the GRP solution as depicted in Fig. 2b, where the right wave is a shock separating two smooth non-uniform flow regions. Denote variables ahead of (resp. behind) the shock by Q_+ (resp. Q). Parametrizing the shock trajectory as $\xi(\theta)$, $t(\theta)$ with $(\xi(0), t(0)) = (0, 0)$, the time-derivative of any flow variable $Q(\xi(\theta), t(\theta))$ along this trajectory is given by

$$\frac{\mathrm{d}Q}{\mathrm{d}\theta} = \left(\frac{\partial Q}{\partial t} + \sigma(\theta)\frac{\partial Q}{\partial \xi}\right) t'(\theta), \tag{3.13}$$

where σ is the Lagrangian shock velocity, given by (3.8). This expression for the time-derivative holds true for flow variables on either side of the shock discontinuity.

To express $\left(\frac{\partial h}{\partial t}\right)^*$ and $\left(\frac{\partial u}{\partial t}\right)^*$ in terms of $\mathbf{V}_R, \mathbf{V}'_R, \mathbf{V}^*, \lambda, S_0, S_f$, we use the interaction-curve relation between the variables on either side of a right shock (3.9), substituting $(h_0, u_0) = (h_+, u_+)$. Since this relation holds for all $t > 0$ along the shock trajectory, we apply the directional derivative (3.13) to the shock interaction curve obtaining

$$\frac{\partial u}{\partial t} + \sigma\frac{\partial u}{\partial \xi} = \frac{\partial u_+}{\partial t} + \sigma\frac{\partial u_+}{\partial \xi} + \Phi_h\left[\frac{\partial h}{\partial t} + \sigma\frac{\partial h}{\partial \xi}\right] + \Phi_{h_+}\left[\frac{\partial h_+}{\partial t} + \sigma\frac{\partial h_+}{\partial \xi}\right]. \tag{3.14}$$

Using the shallow water equations (3.3), we replace the pre-shock time-derivatives by ξ-derivatives, and the post-shock ξ-derivatives by time-derivatives, obtaining

$$\begin{aligned}\frac{\partial u}{\partial t} - \frac{\sigma}{bh^2}\left[\frac{\partial h}{\partial t} + \lambda u h\right] &= -bc_+^2 h'_+ + g[S_0 - S_f]_R + \sigma u'_+ + \Phi_h\left[\frac{\partial h}{\partial t} - \frac{\sigma}{bc^2}\left(\frac{\partial u}{\partial t} - g[S_0 - S_f]\right)\right] \\ &\quad + \Phi_{h_+}\left[-bh_+^2\frac{\partial u_+}{\partial \xi} - \lambda u_+ h_+ + \sigma h'_+\right].\end{aligned} \tag{3.15}$$

In the limit $\theta \to 0$ we get $Q_+ \to Q_R$, $Q \to Q^*$, $b \to b(0)$, $\frac{\partial Q}{\partial t} \to \left(\frac{\partial Q}{\partial t}\right)^*$, $\frac{\partial Q_+}{\partial \xi} \to Q'_R$. Substituting these limits in (3.15), and collecting terms for the three coefficients in (3.12), we finally get for a right shock

$$\begin{aligned}
a_R &= \frac{3}{2} + \frac{0.25}{\eta} + \frac{0.25}{\eta^2}, \quad \eta = h^*/h_R, \\
b_R &= -\left[\frac{g}{2h_R}\right]^{1/2}\left[\eta + 1.5 + \frac{1.5}{\eta}\right][\eta(1+\eta)]^{-1/2}, \\
d_R &= L_h h'_R + L_u u'_R + L_\lambda \lambda + L_S[S_0 - S_f^*] + g[S_0 - S_f]_R, \\
L_h &= -b(0)\frac{c_R^2}{4}[6 + \eta + \eta^2], \\
L_u &= b(0)\kappa_R\frac{[2 + 3\eta + 3\eta^2]}{\sqrt{8\eta(1+\eta)}}, \\
L_\lambda &= \sqrt{\frac{gh_R}{2}}\left[(1+\eta)u^* + \frac{u_R}{2}(2 + \eta + \eta^2)\right]\frac{1}{\sqrt{\eta(1+\eta)}}, \\
L_S &= \frac{g}{4\eta^2}[1 + \eta + 2\eta^2].
\end{aligned} \tag{3.16}$$

This completes the GRP analysis for a right shock. The corresponding expressions for a left shock are readily derived by subjecting (3.16) to the "symmetry reflection" $u \to -u$, $\xi \to -\xi$, $t \to t$, so that u_R, u'_R, h_R, h'_R are replaced by $-u_L$, u'_L, h_L, $-h'_L$, etc.

3.5. GRP analysis of a centered rarefaction wave (CRW)

We reconsider the flow depicted in Fig. 2b, focusing this time on the left-propagating CRW. Unlike a shock wave, a non-self-similar CRW is a continuous flow field for which there exists no "algebraic" relation between the pre-wave and the post-wave states. Hence, deriving expressions for the coefficients a_L, b_L, d_L in (3.12) requires a detailed resolution of the CRW (see [1–3] for the gasdynamical case). In fact, in his pioneering second-order extension to the Godunov method, van Leer [15] circumvented this analysis by resorting to an approximation where a CRW is treated as a "rarefaction shock". This approximation, however, is restricted to weak rarefaction waves (see the analysis in [3, Appendix D]).

Recalling the aforementioned analogy between the shallow water equations and the equations for isentropic flow of an ideal gas, the CRW solution could be obtained by substituting $\gamma = 2$ in the respective gasdynamical solution. However, while this would include the cross-section area term (corresponding to the width $b(x)$ here), it would leave out the bed slope and friction terms, for which there is no analogy in the gasdynamical case. We therefore repeat the GRP analysis for a shallow water CRW including, in particular, the treatment of the bed slope and friction terms. For a detailed discussion of the gasdynamical CRW analysis we refer the reader to [2,3].

Referring to Fig. 3, we set up the characteristic coordinates (α, β) which map the singular (ξ, t) domain into a full rectangle in the (α, β) plane. The coordinate β is defined as the normalized slope of C_- at $\xi = 0$, i.e., $\beta = \kappa/\kappa_L$. In particular, $\beta = 1$ on the head characteristic, $\beta^* = \kappa^*/\kappa_L$ on the tail characteristic. The characteristic coordinate α along a given C_+ curve is the value of the ξ-coordinate at the intersection of C_+ with the head C_- characteristic ($\beta = 1$). Under this setup, $\alpha = 0$ coincides with the singularity $(\xi, t) = (0, 0)$ and the triangular sector of the CRW shown in Fig. 3 is mapped onto the rectangular domain:

$$D \equiv [(\alpha, \beta);\ \bar{\alpha} \leqslant \alpha \leqslant 0,\ 0 < \beta* \leqslant \beta \leqslant 1]. \tag{3.17}$$

Our objective here is to derive expressions for directional derivatives of flow variables at the singularity $\frac{\partial Q}{\partial \alpha}(0, \beta)$ for $(\beta^* \leqslant \beta \leqslant 1)$. For that, all variables, including the coordinates ξ, t, are expressed as functions of α, $\beta \in D$, and evaluated at the singularity $\alpha = 0$. We start by rewriting the characteristic directions (3.6) in terms of (α, β) as

$$\begin{aligned} \frac{\partial \xi}{\partial \alpha} &= -b\kappa \frac{\partial t}{\partial \alpha}, \\ \frac{\partial \xi}{\partial \beta} &= +b\kappa \frac{\partial t}{\partial \beta}. \end{aligned} \tag{3.18}$$

Differentiating the first equation with respect to β and the second with respect to α, and noting that at $\alpha = 0$ the channel width is $b(0, \beta) = b(0)$ and $\frac{\partial t}{\partial \beta}(0, \beta) = \frac{\partial b}{\partial \beta}(0, \beta) = 0$, we obtain

$$\frac{\partial t}{\partial \alpha}(0, \beta) = -\frac{1}{b(0)\kappa_L}\beta^{-1/2}, \quad \text{and} \quad \frac{\partial}{\partial \alpha}\left(\frac{\partial t}{\partial \beta}\right)(0, \beta) = \frac{1}{2b(0)\kappa_L}\beta^{-3/2}. \tag{3.19}$$

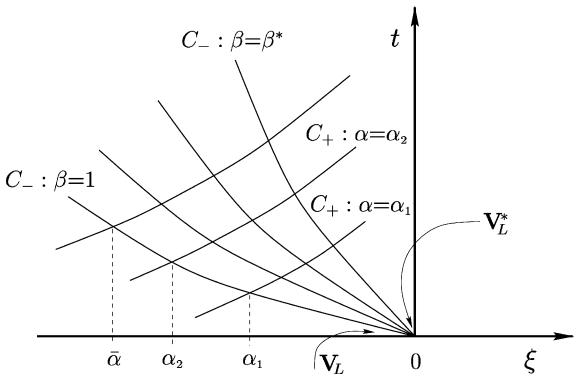

Fig. 3. Characteristic coordinates mapping of a left-facing CRW.

Here we have also used the relations $h(0,\beta)=h_L\beta^{2/3}$, $c(0,\beta)=c_L\beta^{1/3}$, which follow directly from the definitions $c=(gh)^{1/2}$, $\kappa=hc$, $\beta=\kappa/\kappa_L$.

Next we derive the directional derivative of u at the singularity, denoted by $a(\beta)=\frac{\partial u}{\partial\alpha}(0,\beta)$. First we rewrite relations (3.6) as

$$\begin{aligned} &c^2\frac{\partial h}{\partial\alpha}-\kappa\frac{\partial u}{\partial\alpha}+[uc\kappa\lambda+c^3(S_0-S_f)]\frac{\partial t}{\partial\alpha}=0 \quad \text{along } C_-,\\ &c^2\frac{\partial h}{\partial\beta}+\kappa\frac{\partial u}{\partial\beta}+[uc\kappa\lambda-c^3(S_0-S_f)]\frac{\partial t}{\partial\beta}=0 \quad \text{along } C_+. \end{aligned} \tag{3.20}$$

Then we eliminate the derivative $\frac{\partial h}{\partial\alpha}(0,\beta)$ by differentiating the first relation in (3.20) with respect to β and the second with respect to α, taking the difference at $\alpha=0$. Noting that at $\alpha=0$ we have $\frac{\partial\lambda}{\partial\beta}=\frac{\partial S_0}{\partial\beta}=0$, and using once more the characteristic relations (3.20), we get after some algebraic manipulations the following expression for $a'(\beta)$

$$a'(\beta)=-\frac{\lambda}{2b(0)\kappa_L}\beta^{-1/2}\frac{\partial}{\partial\beta}[u(0,\beta)c(0,\beta)]+\frac{c_L}{2b(0)h_L^2}\left[S_0\beta^{-\frac{3}{2}}+\beta^{\frac{1}{2}}\frac{\partial}{\partial\beta}\left(\frac{S_f}{\beta}\right)\right]. \tag{3.21}$$

This relation is supplemented by knowledge of $a(1)$ to yield a unique solution for $a(\beta)$. To evaluate $a(1)$ we use the fact that on the head characteristic C_- $a(1)$ is given solely by the initial conditions at $\xi\to 0-$. By the chain rule

$$a(1)=\frac{\partial u}{\partial\alpha}(0,1)=\frac{\partial u}{\partial\xi}\frac{\partial\xi}{\partial\alpha}(0,1)+\left(\frac{\partial u}{\partial t}\right)_L\frac{\partial t}{\partial\alpha}(0,1).$$

Using (3.19) for the α-derivatives of ξ, t, and (3.3) to replace the t-derivative of u by its ξ-derivative we get

$$a(1)=u_L'+\frac{c_L^2}{\kappa_L}h_L'-\frac{g}{b(0)\kappa_L}(S_0-S_f)_L. \tag{3.22}$$

Performing the integration of elementary functions in (3.21) we get the following expression for $a(\beta)$

$$\begin{aligned} a(\beta)&=a(1)-\int_\beta^1 a'(\bar\beta)\,\mathrm{d}\bar\beta\\ &=u_L'+\frac{c_L^2}{\kappa_L}h_L'+\frac{\lambda}{b(0)h_L}[u_L+2c_L]\left(\beta^{-\frac{1}{6}}-1\right)+\frac{4\lambda c_L}{b(0)h_L}\left(\beta^{\frac{1}{6}}-1\right)-\frac{c_L}{b(0)h_L^2}S_0\beta^{-\frac{1}{2}}\\ &\quad+\frac{c_L}{2b(0)h_L^2}\left[S_f(h_L,u_L)+\beta^{-\frac{1}{2}}S_f(h(\beta),u(\beta))+\frac{1}{2}\int_\beta^1\bar\beta^{-\frac{3}{2}}S_f(h(\bar\beta),u(\bar\beta))\,\mathrm{d}\bar\beta\right]. \end{aligned} \tag{3.23}$$

The finite integral on the right side of (3.23) depends on the specific model for S_f, and generally has to be evaluated numerically. It is often adequate, however, to approximate this finite integral for $1-\beta^*\ll 1$ by the mean-value estimate

$$\int_{\beta^*}^1\beta^{-\frac{3}{2}}S_f(h(\beta),u(\beta))\,\mathrm{d}\beta\approx\frac{1}{2}(1-\beta^*)\left[S_f(h_L,u_L)+(\beta^*)^{-\frac{3}{2}}S_f(h(\beta^*),u(\beta^*))\right]. \tag{3.24}$$

Indeed, in a typical test case (see Section 5.5) it was found that for all times and at all points $1-\beta^*<0.03$.

Once $a(\beta)=\frac{\partial u}{\partial\alpha}(0,\beta)$ is known, the corresponding characteristic slope for h, $\frac{\partial h}{\partial\alpha}(0,\beta)$ is obtained using the characteristic relations (3.20)

$$\frac{\partial h}{\partial\alpha}(0,\beta)=\frac{h(0,\beta)}{c(0,\beta)}a(\beta)-[\lambda h(0,\beta)u(0,\beta)+c(0,\beta)(S_0-S_f)]\frac{\partial t}{\partial\alpha}(0,\beta) \tag{3.25}$$

with $\frac{\partial t}{\partial\alpha}$ given by (3.19).

Having obtained expressions for the α-derivatives of $u(0,\beta)$ and $h(0,\beta)$ in the CRW, we are now in position to derive the coefficients a_L, b_L, d_L. Applying the chain rule to the α-derivative of h along the C_- tail characteristic, we get

$$\frac{\partial h}{\partial \alpha}(0,\beta^*) = \left(\frac{\partial h}{\partial \xi}\right)^* \frac{\partial \xi}{\partial \alpha}(0,\beta^*) + \left(\frac{\partial h}{\partial t}\right)^* \frac{\partial t}{\partial \alpha}(0,\beta^*). \tag{3.26}$$

Using (3.3) to replace the ξ-derivative by t-derivative, and (3.19) for the α-derivatives of ξ and t, produces the expression

$$\frac{\partial h}{\partial \alpha}(0,\beta^*) = -\frac{1}{b(0)\kappa_L \beta^{*1/2}}\left(\frac{\partial h}{\partial t}\right)^* + \left[-\left(\frac{\partial u}{\partial t}\right)^* + g(S_0 - S_f^*)\right]\frac{\beta^{*1/2}}{b(0)c^{*2}}. \tag{3.27}$$

We now eliminate $\frac{\partial h}{\partial \alpha}(0,\beta^*)$ between (3.27) and the relation (3.6) along the C_- tail characteristic, obtaining

$$\left(\frac{\partial u}{\partial t}\right)^* + \frac{(c^*)^2}{\kappa^*}\left(\frac{\partial h}{\partial t}\right)^* = -\frac{\kappa^* b(0)}{(\beta^*)^{1/2}}\left(\frac{\partial u}{\partial \alpha}\right)^* - \lambda u^* c^* + \left[g - \frac{(c^*)^3}{\kappa^*}\right](S_0 - S_f^*). \tag{3.28}$$

Using the definitions of κ, c and the relation $c(0,\beta) = c_L \beta^{1/3}$, it is easily demonstrated that the term proportional to $(S_0 - S_f)$ is identically zero. Hence we get for the left coefficients

$$a_L = 1, \quad b_L = \frac{c^*}{h^*}, \quad d_L = -\kappa_L (\beta^*)^{1/2} b(0) a(\beta^*) - \lambda u^* c^*, \tag{3.29}$$

where $a(\beta^*)$ is given by (3.23). This completes the GRP analysis for a left CRW. The corresponding expressions for a right CRW are readily derived by subjecting (3.29) to the "symmetry reflection" $u \to -u$, $\xi \to -\xi$, $t \to t$, so that u_L, u'_L, h_L, h'_L are replaced by $-u_R$, u'_R, h_R, $-h'_R$, etc.

3.6. Back to the Eulerian framework

From the six coefficients $a_L, b_L, d_L, a_R, b_R, d_R$ (evaluated as explained above) the time-derivatives of u and h at $\xi = 0$, $t \to 0+$ in the Lagrangian coordinates are calculated by solving the linear system of equations (3.12). Recalling that the governing equations and their finite-difference approximation (1.1), (2.1) are in Eulerian coordinates, we must seek the corresponding derivatives along the cell-interface point $x = 0$ in the Eulerian frame of reference. By (2.2) these are the main building blocks of the GRP numerical scheme. The determination of these derivatives depends on the relative position of the line $x(\xi,t) = 0$ at $\xi = 0$ and $t \to 0+$, with respect to the (ξ,t) trajectories of the waves in the solution to the associated Riemann problem. For the particular wave-pattern shown in Fig. 2, the line $x = 0$ is located in one of the six sectors ($\nu = 1,2,3,4,5,6$) shown in Fig. 4 (sector $\nu = 5$ is absent since it can exist only within a CRW, and the right wave in this case is a shock). Sectors $\nu = 1,6$ are to the left or to the right of the respective waves; each one of the sectors $\nu = 3,4$ (separated by the particle path $\xi = 0$) is the mid-state between the left-propagating and the right-propagating waves. The distinction between sectors $\nu = 3$ and $\nu = 4$ is required for the SGM modification to be discussed later. Sector $\nu = 2$ is a left CRW, and sector $\nu = 5$ is a right CRW (not shown in Fig. 4).

In sectors $\nu = 1,3,4,6$, referred to as "non-sonic" cases, the Eulerian time-derivatives are obtained using a $(\xi,t) \to (x,t)$ transformation. For the "sonic" cases ($\nu = 2,5$) the ξ,t derivatives are unbounded at

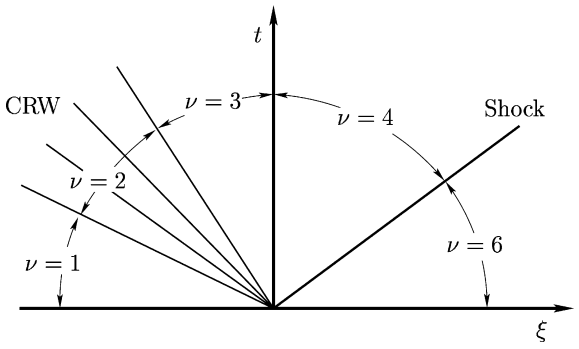

Fig. 4. Image of $x = 0$ line in (ξ,t) solution to associated RP.

$(\xi, t) = (0, 0)$, and the Eulerian time-derivatives must be obtained using the characteristic coordinates that resolve the CRW. Hence, in the following the sonic and non-sonic cases are treated separately.

3.6.1. Nonsonic case

In the (ξ, t) plane the line $x = 0$ is represented by the curve $\xi = \xi(t)$, $\xi(0) = 0$, obtained by differentiating the identity $x(\xi(t), t) = 0$ and using definition (3.1),

$$\xi'(t) = -b(0)h(\xi, t)u(\xi, t), \quad \xi(0) = 0. \tag{3.30}$$

For any flow variable Q, the transformation $Q(\xi, t) \to Q(x, t)$ at the cell-interface point $(x, t) = (0, 0+)$ is given by

$$\left(\frac{\partial Q}{\partial t}\right)_0 = \left.\frac{\partial Q(x,t)}{\partial t}\right|_{x=0,t=0+} = \left[\frac{\partial Q(\xi,t)}{\partial t} - b(0)h(0,t)u(0,t)\frac{\partial Q(\xi,t)}{\partial \xi}\right]_{\xi=\xi(t),t=0+}, \tag{3.31}$$

where $\xi = \xi(t)$ is the parametric representation (3.30) of the cell-interface point $x = 0$.

When $x = 0$ is in sectors $v = 3, 4$, the time-derivatives are

$$\left(\frac{\partial Q}{\partial t}\right)_0 = \left(\frac{\partial Q}{\partial t}\right)^* - b(0)h^*u^*\left(\frac{\partial Q}{\partial \xi}\right)^*, \tag{3.32}$$

where $(\cdot)^*$ denotes mid-state (sectors $v = 3, 4$) variables, taken as functions of (ξ, t). Applying (3.32) to the variables u, h, and using the (Lagrange) governing equations (3.3) to replace ξ-derivatives by t-derivatives, we obtain (for $x = 0$ in Sectors $v = 3, 4$) the following expressions:

$$\begin{aligned}
\left(\frac{\partial u}{\partial t}\right)_0 &= \left(\frac{\partial u}{\partial t}\right)^* + \frac{u^*}{h^*}\left(\frac{\partial h}{\partial t}\right)^* + \lambda(u^*)^2, \\
\left(\frac{\partial h}{\partial t}\right)_0 &= \left(\frac{\partial h}{\partial t}\right)^* + \frac{u^*}{g}\left(\frac{\partial u}{\partial t}\right)^* - u^*(S_0 - S_f)^*.
\end{aligned} \tag{3.33}$$

If $x = 0$ is in sectors $v = 1$ or $v = 6$, the time-derivatives are obtained directly from the transformation (3.31) and the governing equations (3.3).

$$\begin{aligned}
\left(\frac{\partial u}{\partial t}\right)_0 &= -b(0)u_{LR}h_{LR}\left(\frac{\partial u}{\partial \xi}\right)_{LR} - b(0)gh_{LR}\left(\frac{\partial h}{\partial \xi}\right)_{LR} + g(S_0 - S_f)_{LR}, \\
\left(\frac{\partial h}{\partial t}\right)_0 &= -b(0)(h_{LR})^2\left(\frac{\partial u}{\partial \xi}\right)_{LR} - b(0)u_{LR}h_{LR}\left(\frac{\partial h}{\partial \xi}\right)_{LR} - \lambda u_{LR}h_{LR},
\end{aligned} \tag{3.34}$$

where $(\cdot)_{LR}$ denotes the left ($v = 1$) or the right ($v = 6$) sector.

3.6.2. Sonic case

In this case, (3.31) is meaningless and we resort to the characteristic coordinates (α, β) in a rarefaction fan as introduced in Section 3.5 above. The idea is to express all variables in the CRW sector in terms of (α, β). In particular, the line $x = 0$ is represented by the parametric curve $\alpha(t), \beta(t)$ with $\alpha(0), \beta(0) = (0, \beta_s)$, $\beta^* \leqslant \beta_s \leqslant 1$ (geometrically, it means that the line is tangent to the C_- characteristic $\beta = \beta_s$). To determine β_s, recall that for this characteristic line $\frac{dx}{dt} = u - c = 0$, hence $u = c$ (justifying the term "sonic"). Combining the definition $\beta = \kappa/\kappa_L$, $\kappa = (gh^3)^{1/2}$, and the Riemann invariant relation (3.7), we get

$$\beta_s = \left[\frac{u_L + 2c_L}{3c_L}\right]^3. \tag{3.35}$$

Now, we employ the parametric representation $x(\alpha(t), \beta(t)) = 0$ for the cell-interface point in the CRW, so that by the chain rule Eq. (3.32) is replaced by

$$\left(\frac{\partial Q}{\partial t}\right)_0 = \frac{\partial Q}{\partial \alpha}(0, \beta_s)\alpha'(0) + \frac{\partial Q}{\partial \beta}(0, \beta_s)\beta'(0). \tag{3.36}$$

The terms on the right side of (3.36) are either known, or can be derived from the resolution of the CRW in Section 3.5 above. In particular, $\alpha'(0)$ and $\beta'(0)$ are given by

$$\begin{aligned}\alpha'(0) &= -b(0)\kappa_{\mathrm{L}}\beta_s^{1/2},\\ \beta'(0) &= \frac{1}{2}b(0)\beta_s^{1/2}\left[\frac{\partial(hc)}{\partial\alpha}(0,\beta_s) - \frac{\partial(hu)}{\partial\alpha}(0,\beta_s)\right].\end{aligned} \tag{3.37}$$

Regarding $t(\alpha,\beta)$ as a function along $(\alpha(t),\beta(t))$ we differentiate the identity $t = t(\alpha(t),\beta(t))$ with respect to t. Using (3.19), we get at $t = 0$

$$1 = \frac{\partial t}{\partial\alpha}(0,\beta_s)\alpha'(0) + \frac{\partial t}{\partial\beta}(0,\beta_s)\beta'(0) = -[b(0)\kappa_{\mathrm{L}}\beta_s^{1/2}]^{-1}\alpha'(0),$$

which proves the first equation in (3.37). The detailed derivation of the second equation may be found in [1,2] or [3], and since it is more involved we omit it here. Using (3.37), the sonic condition $u(\beta_s) = c(\beta_s)$ and the characteristic relations (3.6), we get

$$\beta'(0) = -\frac{\beta_s^{1/2}}{4}h(\beta_s)b(0)\frac{\partial u}{\partial\alpha}(0,\beta_s) + \frac{\beta_s}{2}\left[\lambda u(\beta_s) - \frac{c_{\mathrm{L}}}{h_{\mathrm{L}}}\beta_s^{-1/3}(S_0 - S_{\mathrm{f}})\right], \tag{3.38}$$

where all terms on the right are known functions of β_s. In particular, $\partial u/\partial\alpha$ at $(0,\beta_s)$ is obtained by taking $\beta = \beta_s$ in (3.23). From the explicit expression $h = h_{\mathrm{L}}\beta^{2/3}$ we obtain the derivative

$$\frac{\partial h}{\partial\beta}(0,\beta_s) = \frac{2}{3}h_{\mathrm{L}}\beta_s^{-1/3}. \tag{3.39}$$

The corresponding derivative for u is obtained by using the characteristic relations (3.6)

$$\frac{\partial u}{\partial\beta}(0,\beta_s) = -\frac{2}{3}\frac{c_0}{\beta_s} + \lambda\frac{c_{\mathrm{L}}}{h_{\mathrm{L}}}\beta_s^{1/6} - \frac{c_{\mathrm{L}}}{h_{\mathrm{L}}^2}\beta_s^{-1/2}(S_0 - S_{\mathrm{f}}), \tag{3.40}$$

and $\frac{\partial h}{\partial\alpha}$ is given by (3.25).

Substituting u or h for Q in (3.36), and using the foregoing expressions for $\alpha'(0)$, $\beta'(0)$ and the partial derivatives of u,h with respect to α,β, we get the necessary time-derivatives in the sonic case.

4. The GRP numerical scheme

The outline of the GRP scheme for the shallow water system (1.1) given in Section 1, was followed by a presentation of the analytic components of the method in Sections 2 and 3. Here we complete the scheme description by giving a step-by-step account of the shallow water GRP computational algorithm. The time-integration cycle of the conservation laws from t^n to t^{n+1} according to (2.1), (2.2) starts (Section 4.1) by updating the former (t^{n-1}) slopes to the present initial time-level (t^n), and is followed by subjecting these slopes to monotonicity constraints (Section 4.2). In order to obtain the well-balanced property, the height (h) slopes are given in terms of water-level ($\zeta = h + Z$) slopes (Section 4.3). The GRP data is then set up at all cell-boundaries (Section 4.4), and the solution to each associated Riemann problem is evaluated by an iterative solver (Section 4.5). The solution to the GRP at cell-boundaries in the Eulerian system is then evaluated (Section 4.6), leading to the completion of the computational cycle by evaluation of the time-centered fluxes (2.2) and the finite-difference integration according to (2.1).

4.1. Slope updating

The GRP method is based on a piecewise-linear approximation of flow variables per cell. An auxiliary state variable "slope" defined as the difference in the cell endpoints values is introduced, say ΔQ_i^n for the variable Q_i^n in cell i at time t^n. At the beginning of the integration cycle $t^n \to t^{n+1}$ the slopes are updated by the finite-difference relation

$$\Delta Q_i^n = \Delta Q_i^{n-1} + (t^n - t^{n-1})\left[\left(\frac{\partial Q}{\partial t}\right)_{i+\frac{1}{2}}^{n-1} - \left(\frac{\partial Q}{\partial t}\right)_{i-\frac{1}{2}}^{n-1}\right], \tag{4.1}$$

where it is noted that the former integration cycle was $t^{n-1} \to t^n$. The time-derivatives at the cell-boundaries $i-\frac{1}{2}, i+\frac{1}{2}$ in (4.1) were derived by the GRP analysis (Section 3.6).

4.2. Slope limiting

We employ the slope limiter suggested by van Leer [15], which is designed to assure monotonicity of the five-point sequence $[Q_{i-1}^n, Q_{i-\frac{1}{2}}^n, Q_i^n, Q_{i+\frac{1}{2}}^n, Q_{i+1}^n]$. The limiting algorithm can be written as

$$\Delta Q_i^n = \text{minmod}\left[\Delta Q_i^n, 2(Q_i^n - Q_{i-1}^n), 2(Q_{i+1}^n - Q_i^n)\right]. \tag{4.2}$$

Following the slope limiting, cell-boundary values are evaluated by

$$Q_{i+\frac{1}{2},\mathrm{L}}^n = Q_i^n + \frac{1}{2}\Delta Q_i^n, \quad Q_{i+\frac{1}{2},\mathrm{R}}^n = Q_{i+1}^n - \frac{1}{2}\Delta Q_{i+1}^n, \tag{4.3}$$

and serve as part of the GRP data at $x_{i+\frac{1}{2}}$ (indices L, R denote left,right side of the cell-boundary point, respectively).

4.3. Balancing of gravitation source terms

The gravitational source term in **H** (1.1) raises an issue of "source–flux balancing", as pointed out by LeVeque [12]. By "imbalance" we refer to the truncation error obtained in the case of a quiescent flow IVP with varying bed elevation (i.e., $u(x,0) = 0$, $h(x,0) + Z(x) = \text{constant}$, while $Z(x)$ is non-uniform). In order to meet the "well balanced" property, the foregoing procedures for slope updating and limiting are applied to the flow variables u and $\zeta = h + Z$, rather than to u and h. The h slopes are then recovered by $\Delta h = \Delta\zeta - \Delta Z$ as in the SGM method [17].

First, the bed elevation is discretized as piecewise-linear in cells, with mid-cell values taken as the average of cell-boundary values, i.e.,

$$\begin{aligned} Z_{i+\frac{1}{2}} &= Z(x_{i+\frac{1}{2}}), \\ Z_i &= \frac{1}{2}(Z_{i-\frac{1}{2}} + Z_{i+\frac{1}{2}}), \\ \Delta Z_i &= Z_{i+\frac{1}{2}} - Z_{i-\frac{1}{2}}. \end{aligned} \tag{4.4}$$

Then, the discretized water level at the initial time level t^n is set up as

$$\zeta_i^n = h_i^n + Z_i, \tag{4.5}$$

and the slopes of h are updated to t^n according to (4.1), *without subjecting them to the monotonicity constraints (4.2)*. Now we express the updated ζ slopes as

$$\Delta\zeta_i^n = \Delta h_i^n + \Delta Z_i, \tag{4.6}$$

and subject $\Delta\zeta_i^n$ to the monotonicity constraint (4.2). The procedure is concluded by deriving the updated h slopes as

$$\Delta h_i^n = \Delta\zeta_i^n - \Delta Z_i. \tag{4.7}$$

The slope integration and subsequent limiting are thus performed for Δu_i^n, $\Delta\zeta_i^n$ according to (4.1), (4.2), and the slopes Δh_i^n are then given by (4.7) above. The key idea is that Δh_i^n should not be subjected to the monotonicity constraints, so that in the equilibrium case where $\zeta = \text{constant}$ and $\Delta\zeta = 0$, the slopes for h would adhere exactly to the bed slopes, i.e., $\Delta h_i^n = -\Delta Z_i$.

4.4. GRP data at cell-boundaries

The GRP data (see Section 3.3) consists of the values of flow variables on either side of cell boundaries, along with the respective gradients. The data for the associated Riemann problem consists of the values of h, u on either side of the grid point, obtained by extrapolation of mid-cell values according to (4.3). For maintaining the well-balanced property (SGM modification), the bed profile gradients at cell boundaries $x_{i+\frac{1}{2}}$ are given not by $Z'(x_{i+\frac{1}{2}})$, but rather by those of the piecewise-linear profile (4.4), i.e.,

$$\begin{aligned}\left(\frac{\partial Z}{\partial x}\right)_{i+\frac{1}{2},\mathrm{L}} &= -(S_0)_{i+\frac{1}{2},\mathrm{L}} = \frac{\Delta Z_i}{\Delta x_i},\\ \left(\frac{\partial Z}{\partial x}\right)_{i+\frac{1}{2},\mathrm{R}} &= -(S_0)_{i+\frac{1}{2},\mathrm{R}} = \frac{\Delta Z_{i+1}}{\Delta x_{i+1}}.\end{aligned} \tag{4.8}$$

Thus, the bed slope values S_0 appearing in the GRP analysis of Chapter 3 should be replaced by the corresponding "one-sided" slopes given in (4.8).

The point-centered values of flow variables are given by substituting u or h in (4.3). The ξ-gradients required in the GRP analysis are approximated by the finite-difference expressions

$$\begin{aligned}\left(\frac{\partial u}{\partial \xi}\right)_{i+\frac{1}{2},\mathrm{L}} &= \frac{\Delta u_i}{h_{i+\frac{1}{2},\mathrm{L}}\Delta s_i}, \quad \left(\frac{\partial u}{\partial \xi}\right)_{i+\frac{1}{2},\mathrm{R}} = \frac{\Delta u_{i+1}}{h_{i+\frac{1}{2},\mathrm{R}}\Delta s_{i+1}},\\ \left(\frac{\partial h}{\partial \xi}\right)_{i+\frac{1}{2},\mathrm{L}} &= \frac{\Delta h_i}{h_{i+\frac{1}{2},\mathrm{L}}\Delta s_i}, \quad \left(\frac{\partial h}{\partial \xi}\right)_{i+\frac{1}{2},\mathrm{R}} = \frac{\Delta h_{i+1}}{h_{i+\frac{1}{2},\mathrm{R}}\Delta s_{i+1}},\end{aligned} \tag{4.9}$$

where Δs_i is the channel area integral given in (2.1).

4.5. Solution of associated Riemann problem

Let the associated Riemann problem data obtained by (4.3) be $\mathbf{V}_\mathrm{L} = [h_\mathrm{L}, u_\mathrm{L}]^\mathrm{T}$, $\mathbf{V}_\mathrm{R} = [h_\mathrm{R}, u_\mathrm{R}]^\mathrm{T}$, for the left,-right sides of a grid point, respectively. The solution to this RP is the mid-state $\mathbf{V}^* = [h^*, u^*]^\mathrm{T}$, as explained in Section 3.2. The algorithm for computing $\mathbf{V}^*$ is readily formulated as follows. Let the left,right interaction curves be $u(h) = I_\mathrm{L}(h)$, $u(h) = I_\mathrm{R}(h)$, respectively. Each curve consists of a rarefaction branch (Eq. (3.7)) and a shock branch (Eq. (3.9)). Interaction curves are monotonically increasing (right), or monotonically decreasing (left). This enables pre-determination of the branch on which the intersection point $\mathbf{V}^*$ lies. For example, if $h_\mathrm{R} < h_\mathrm{L}$ then $I_\mathrm{L}(h_\mathrm{R}) > u_\mathrm{R}$ implies that $\mathbf{V}^*$ lies on the shock branch of $I_\mathrm{R}(h)$, and so on (see [3, Appendix C]). Once the branches are known, the actual value of $\mathbf{V}^*$ is readily calculated by the Newton–Raphson iterative method. We also note that since the shallow water Riemann problem can be readily solved as outlined here, there is no incentive to seek an approximate Riemann solver.

4.6. The Eulerian GRP solution

Once the associated RP at a cell boundary point has been solved, the solution of the respective GRP is given in terms of the time-derivatives of u^* and h^* along the "contact path" $\xi'(t) = u^*$. These are obtained by solving the pair of linear equations (3.12) that express the "second-order coupling" between the left-side and right-side waves. Mapping back to the Eulerian framework, as outlined in Section 3.6, we evaluate the time-derivatives of $\mathbf{U}$ and the time-centered variables $\mathbf{U}_{i+\frac{1}{2}}^{n+\frac{1}{2}}$ and fluxes $\mathbf{F}(\mathbf{U})_{i+\frac{1}{2}}^{n+\frac{1}{2}}$, $\mathbf{G}(\mathbf{U})_{i+\frac{1}{2}}^{n+\frac{1}{2}}$ according to (2.2). The mid-cell time-centered value of $\mathbf{H}$ is expressed implicitly as $\mathbf{H}(\mathbf{U}_{i+\frac{1}{2}}^{n+\frac{1}{2}})$ with $\mathbf{U}_{i+\frac{1}{2}}^{n+\frac{1}{2}} = \frac{1}{2}(\mathbf{U}_i^n + \mathbf{U}_i^{n+1})$, requiring a predictor-corrector iteration of the time-integration (2.1). This completes the setup for calculating the time-integrated values according to the GRP finite-difference approximation (2.1), (2.2).

5. Numerical examples

The GRP scheme presented here is designed to solve numerically the one-dimensional shallow water equations that govern unsteady flow in rectangular cross-section channel (1.1). These equations contain terms due to a smoothly varying channel width and bed elevation, as well as a term modeling the shear stress at the wetted perimeter. The five examples considered here contain various combinations of these terms, and refer to either steady or unsteady flow, as summarized in Table 1.

In the following we discuss separately each of the five examples, using for the numerical computation an equally spaced grid and a constant time step complying with the Courant–Friedrichs–Levy stability condition. We note that units are everywhere in the *MKS* system unless otherwise specified. In all cases the computed results are shown as points, and the exact or accurate distribution is shown as a line-curve.

5.1. Planar dam break

Consider the flow resulting from an abrupt breach of a dam separating the two uniform states: $[h_l, u_l] = [10, 0]$ on the left and $[h_r, u_r] = [0.1, 0]$ on the right. The computational domain $[0, 2000]$ was divided into an equally spaced grid of 100 cells, with the dam located at the mid-point $x = 1000$. The constant time step was $\Delta t = 1.25$, corresponding to a CFL ratio of $(c + |u|)\Delta t/\Delta x \approx 1$, and the computation was performed to the final time of $t = 50$. The channel width was $b(x) = 1$ and the source terms related to bed profile and friction vanished ($\mathbf{H} = \mathbf{0}$).

This initial value problem for (1.1) is known as a Riemann problem and its exact (self-similar) solution is readily obtainable (Section 3.2). The flow field consists of a right-facing shock and a left-facing rarefaction. The computed depth and velocity are shown in Fig. 5, where the smooth line is the exact solution.

Table 1
Features of the numerical examples

Example	Steady flow	Varying width	Varying elevation	Friction
1. Planar dam break	No	No	No	No
2. Radial dam break	No	Yes	No	No
3. LeVeque's test	No	No	Yes	No
4. Channel flow I	Yes	Yes	No	No
5. Channel flow II	Yes	Yes	Yes	Yes

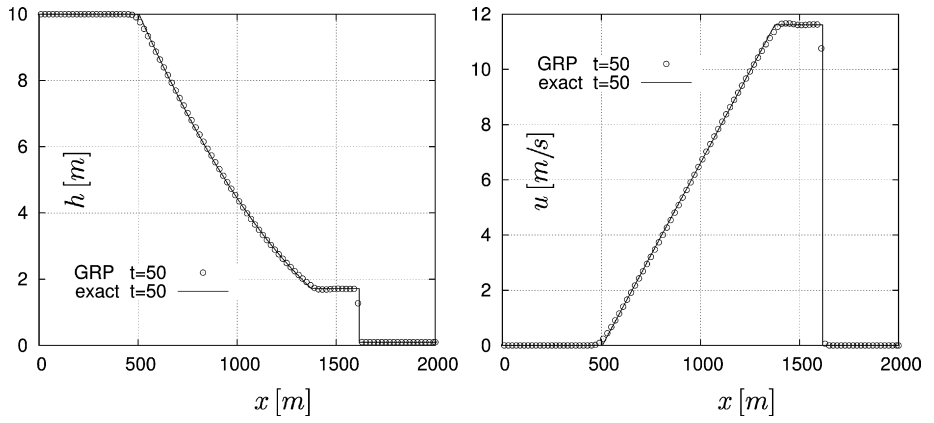

Fig. 5. Planar dam break: water level and velocity.

This is a severe test problem since the relatively high initial depth ratio of 100:1 produces a strong rarefaction wave with a transition from subcritical to supercritical flow at the location of the collapsed dam ($x = 1000$). At this sonic point the flow is critical, and some numerical schemes were found to erroneously produce a discontinuous solution (see [18]). The GRP results (Fig. 5) adhere quite well to the exact solution and in particular are smooth at the sonic point.

In a survey of explicit numerical schemes, Zoppou and Roberts [18] have used this dam break problem for an accuracy test, with an L_1 error norm defined as

$$L_1 = \frac{\sum_{j=1}^{k} |c_j - C_{\text{exact}}(x_j)|}{\sum_{j=1}^{k} |C_{\text{exact}}(x_j)|}, \tag{5.1}$$

where c_j is the numerical solution at node j and $C_{\text{exact}}(x_j)$ is the corresponding exact solution. That survey was conducted with 100 computational cells, as in our test run here. Based on norm (5.1), a scheme figure of merit L_1^I was defined as the following inverse norm ratio

$$L_1^I = L_{1(\text{Lax–Friedrichs})}/L_{1(\text{Scheme})},$$

where the values of the Lax–Friedrichs norm were $L_1 = 0.0476$ for the water-depth and $L_1 = 0.186$ for the velocity. The values of inverse norms obtained for the present GRP scheme and for the direct-Eulerian version [13] (we thank the authors for the numerical data) were in the range of 9–10 for h and 17–20 for u; small differences between the two schemes were due to secondary features such as slope monotonization. The inverse norms obtained for other explicit schemes [18] were no higher than about 1/3 of the respective GRP values.

5.2. Radial dam break

Our quasi-one-dimensional scheme is now applied to the two-dimensional flow resulting from an abrupt breach of a circular dam confining a cylindrical body of water. The initial data, grid spacing, final time are taken to be those of Zoppou and Roberts [19], who computed this flow in a rectangular domain using the 2D WAF scheme [5]. Here the computation domain $[0, 100]$ is divided into an equally spaced grid of 100 cells. The time step is $\Delta t = 0.05$, and the computation is performed to the final time of $t = 2$. Radial symmetry is obtained in our 1D setting by taking $b(x) = 2\pi x$.

Contrary to the planar dam break, this problem has no exact solution. Therefore, $h(x, 2)$ and $Fn(x, 2)$ computed with 100 cells are shown in Fig. 6 along with the corresponding profiles obtained by a highly resolved computation (1000 cells). Note that the finite-difference integration of the flux term $b(x)\mathbf{F}$ in (2.1) is fully incorporated into the GRP conservation laws formulation, whereas some other 1D schemes (e.g., [19,5]) are formulated as plane-symmetric conservation laws, where the added "geometrical source term" $[b'(x)/b(x)]\mathbf{F}$ requires a time-split integration.

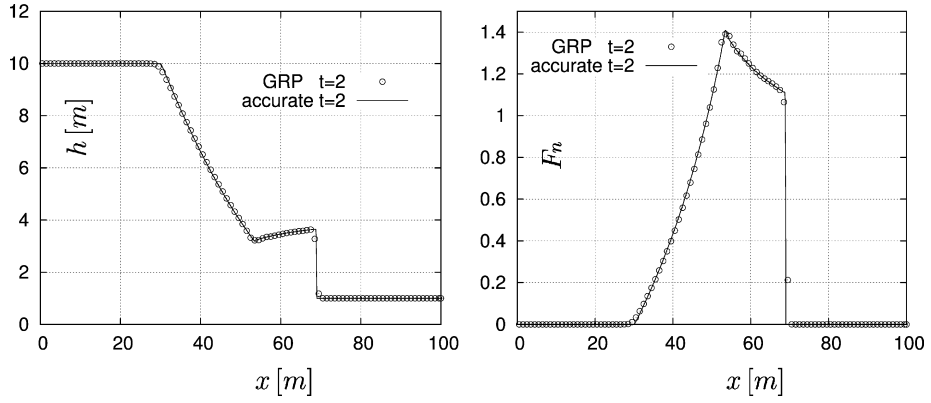

Fig. 6. Radial dam break: water level and Froude number.

5.3. LeVeque's perturbation test

In this test problem [12] a localized initial perturbation of the water surface level produces waves that later interact with the steep channel bed profile:

$$Z(x) = \begin{cases} 0.25[\cos(\pi(x-0.5)/0.1)+1] & \text{if } |x-0.5| < 0.1, \\ 0 & \text{otherwise.} \end{cases} \tag{5.2}$$

The initial data is a quiescent state with a flat water level perturbed by the localized square-wave

$$\zeta(x) = h(x) + Z(x) = \begin{cases} 1+\epsilon & \text{if } 0.1 < x < 0.2, \\ 1 & \text{otherwise.} \end{cases} \tag{5.3}$$

Here system (1.1) is solved for a channel of constant width, a gravity acceleration $g = 1$, and two levels of perturbation: $\epsilon = 0.01$, $\epsilon = 0.20$. The computational domain $[0,1]$ is divided into an equally spaced grid of 100 cells, the time step is $\Delta t = 0.001$, and the computation is performed to the final time of $t = 0.7$. The water surface level at the initial and final times for $\epsilon = 0.01$ and $\epsilon = 0.20$ are shown in Figs. 7 and 9, respectively. The velocity profile and the enhanced-scale water surface level profile for the two perturbation values are shown in Figs. 8 and 10, along with reference curves obtained by a well-resolved computation (1000 cells). In order to avoid reliance on "non-reflecting boundary conditions" at $x = 0$ we have extended the computation domain to $[-1,1]$, keeping the same mesh size 0.01 (in the figures only the interval $0 < x < 1$ is shown). Our results for the two test cases are comparable to those of LeVeque [12] and Li and Chen [13]. We have also rerun the problem for the zero-perturbation case ($\epsilon = 0$), obtaining exactly the flat-surface solution ($[h,u] = [1,0]$) at $t = 0.7$. Our

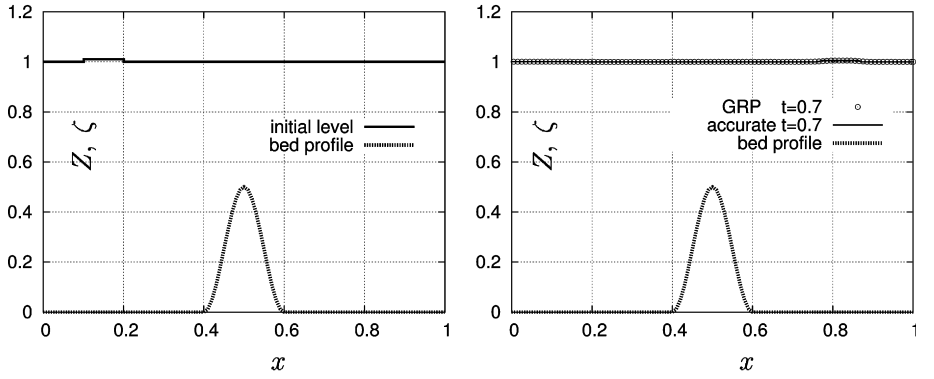

Fig. 7. LeVeque's perturbation test $\epsilon = 0.01$: water level and bed profile.

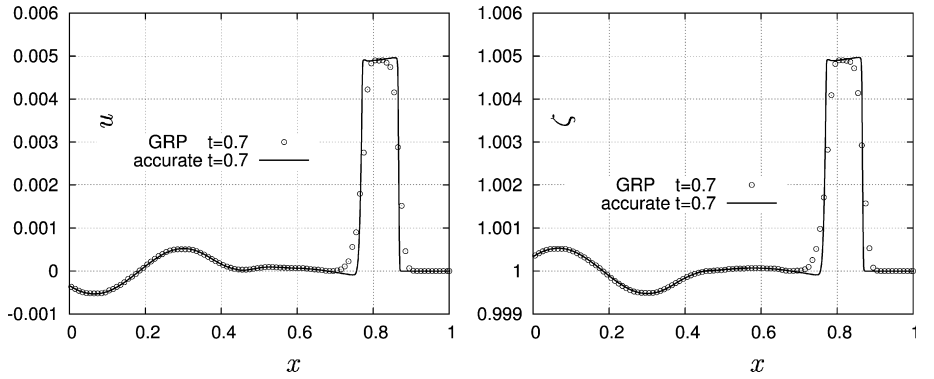

Fig. 8. LeVeque's perturbation test $\epsilon = 0.01$: water level and velocity.

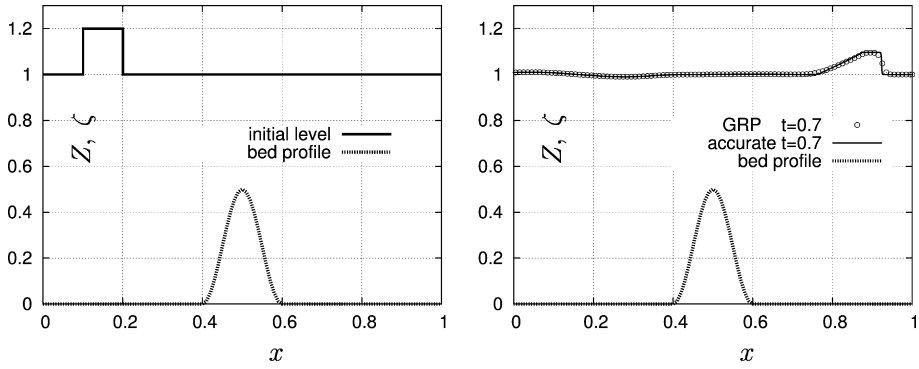

Fig. 9. LeVeque's perturbation test $\epsilon = 0.20$: water level and bed profile.

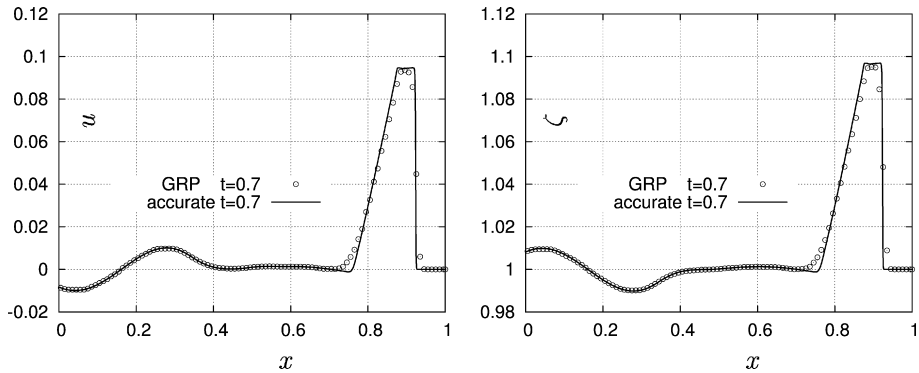

Fig. 10. LeVeque's perturbation test $\epsilon = 0.20$: water level and velocity.

verification was by simply inspecting the computed values of the velocity, which was found to be zero to within the digital round-off error ($\approx 10^{-12}$). This confirms that our finite-difference GRP scheme (2.1) is well-balanced.

5.4. Channel flow I

Consider the flow in an open converging–diverging channel with a flat bed and zero shear stress. Let the width function in the interval $[0, 1000]$ be given by

$$b(x) = 10 - 64\left[\left(\frac{x}{1000}\right)^2 - 2\left(\frac{x}{1000}\right)^3 + \left(\frac{x}{1000}\right)^4\right] \tag{5.4}$$

as shown in Fig. 11.

The exact solution is readily obtained by integrating the governing equations for steady smooth flow in a flat channel of variable width. As function of the flow Froude number, the solution for the water depth is given by

$$h = h_o\left(1 + \frac{1}{2}Fn^2\right)^{-1}, \tag{5.5}$$

with h_o denoting the depth at a virtual cross-section where the Froude number vanishes. Thus, the solution for the smooth part of the flow is readily obtained in a parametric form as function of the Froude number. In a flow containing a hydraulic jump, this "isentropic flow" solution is valid separately on either side of the jump (with different values of h_o). Assuming a hydraulic jump at the diverging part of the channel, and using the

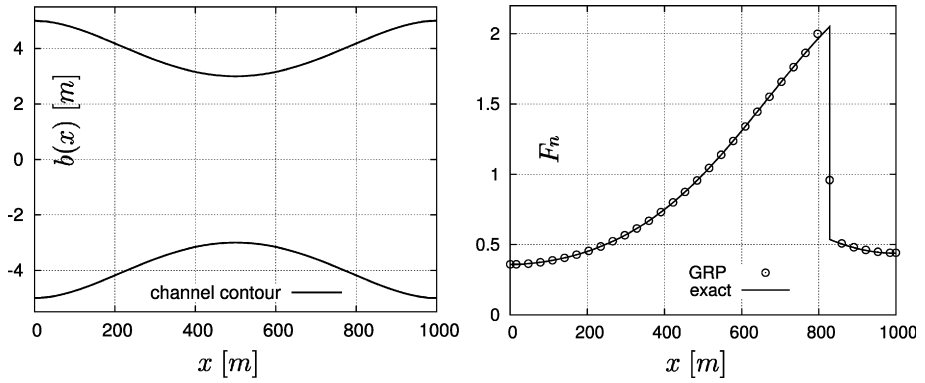

Fig. 11. Channel flow I: width contour $b(x)$, and Froude number at large time.

appropriate jump conditions, our particular solution is obtained for the following conditions. Flow entry depth $h(0,t) = 1.4691$, discharge value $Q = 20\ \mathrm{m}^3/\mathrm{s}$, exit water depth $h(1000,t) = 1.2850$. By iteratively matching the given exit water depth, this solution is found to contain a hydraulic jump at $x = 828.43$. The obtained flow thus accelerates smoothly from subcritical to supercritical in the domain $0 < x < 828.43$, going through critical speed ($Fn = 1$) at the throat ($x = 500$). At $x = 828.43$ the flow undergoes transition to subcritical through a hydraulic jump, as indicated by the (exact) Froude number profile shown in Fig. 11.

The initial conditions for the numerical solution are the smooth profiles $h(x,0) = 1.4691$ and $u(x,0) = Q/(b(x)h(x,0))$. The boundary conditions prescribed at the entry point are the exact depth $h(0,t) = 1.4691$ and velocity $u(0,t) = Q/h(0,t)$, while at the exit point only the exact depth $h(1000,t) = 1.2850$ is prescribed. The steady-state profiles of Fn, h, u, computed with equally spaced 32 computational cells are shown in Figs. 11, 12, and agree well with the exact solution. Note that, although the width $b(x)$ and the initial values of the flow variables $h(x,0)$, $u(x,0)$ are smooth functions of x, the hydraulic jump, which is part of the steady-state solution, is produced by the time-integration to large time. The present example is quite similar to a converging–diverging steady channel flow with hydraulic jump calculated by Garcia-Navarro et al. [8] and later by Vázquez-Céndon [16]. Our scheme, however, calculates this problem without using an extra dissipation step as in [8], or a modified discretization of source terms as in [16].

5.5. Channel flow II

This steady flow problem was devised by MacDonald et al. [14] as a benchmark for numerical schemes. It contains the full array of source terms in the shallow water equations (1.1), i.e., varying channel width, varying

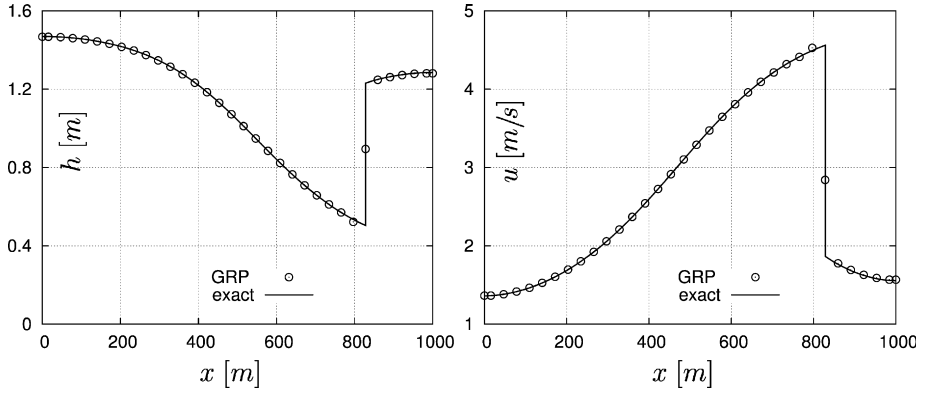

Fig. 12. Channel flow I: water depth and velocity at large time.

bed elevation, and friction. By MacDonald's method, the steady flow solution to (1.1) is constructed in a "reversed" way. First, the channel contour $b(x)$, water depth profile $h(x)$, and friction model (S_f as function of flow variables) are selected. Then, the flow velocity $u(x)$ and the bed profile $Z(x)$ are determined as steady solution to (1.1).

For the present test problem the width contour $b(x)$ is taken as that of the former example (Eq. (5.4), see also Fig. 11).

The depth profile, containing a hydraulic jump at the channel mid-point, is then specified as function of x by

$$h(x) = \begin{cases} -\frac{1}{40} + \left[1 + 2\left(\frac{x}{1000} - \frac{1}{2}\right)^2\right]^{-1} & 0 \leqslant x \leqslant 500, \\ a_0 \exp\left(\frac{x}{4000} - \frac{1}{4}\right) + \sum_{k=1}^{3} a_k \exp\left(15k - 30k\frac{x}{1000}\right) & 500 < x \leqslant 1000, \end{cases} \tag{5.6}$$

where $a_0 = 1.5$, $a_1 = -0.230680$, $a_2 = 0.248267$, $a_3 = -0.228271$.

The dimensionless friction term S_f is modeled by the Manning formula

$$S_f(x,t) = \eta^2 u(x,t)|u(x,t)|\left(\frac{2}{b(x)} + \frac{1}{h(x,t)}\right)^{4/3}, \tag{5.7}$$

where η is the empirical Manning resistance coefficient.

Next, the steady flow velocity is expressed in terms of the steady discharge relation $u(x) = Q/b(x)h(x)$. Now, by reducing the momentum equation in (1.1) to the steady case, the following expression for the bed slope $S_0(x)$ is obtained

$$S_0(x) = S_f(x) + \left(1 - \frac{u^2(x)}{gh(x)}\right)h'(x) - \frac{u^2(x)}{g}\frac{b'(x)}{b(x)}, \tag{5.8}$$

where $S_f(x)$ is the steady version of (5.7). Finally, the bed elevation $Z(x)$ is obtained by quadrature from the relation $Z'(x) = -S_0(x)$ (with $Z(1000) = 0$), where $S_0(x)$ is given by (5.8).

The particular data for the present test case is a flow discharge rate of $Q = 20$ [m^3/s] and a Manning resistance coefficient $\eta = 0.02$ [s/m$^{\frac{1}{3}}$]. The exact bed elevation and water surface level for the resulting flow are shown in Fig. 13, where we also show the exact and computed distributions of the Froude number. The computation was performed on a grid obtained by dividing the interval $[0, 1000]$ into 39 cells of equal length. The initial conditions were $h(x,0) = 1.5$ and $u(x,0) = Q/b(x)h(x,0)$. The boundary conditions consisted in prescribing the exact values of h at the two endpoints, and the exact value of u at the left endpoint ($x = 0$). The time step was $\Delta t = 1.6$ (the CFL stability condition would limit the time step to $\Delta t \approx 3.2$) and the integration was performed to the (large) time $t = 2000$, obtaining steady results. The computed distributions for the water depth h and velocity u are shown in Fig. 14, and agree well with the exact solution.

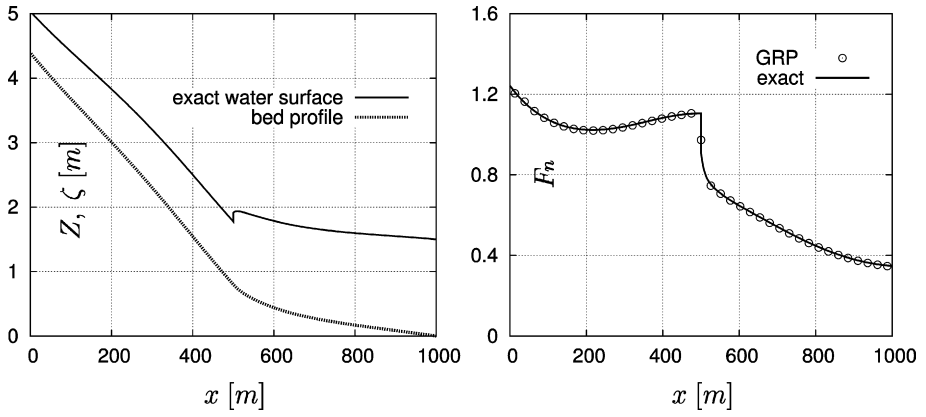

Fig. 13. Channel flow II: bed profile, water level, and Froude number at large time.

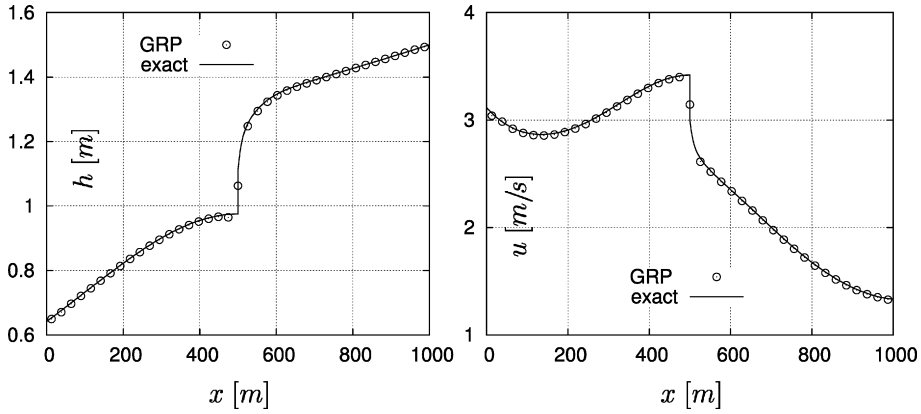

Fig. 14. Channel flow II: water depth and velocity at large time.

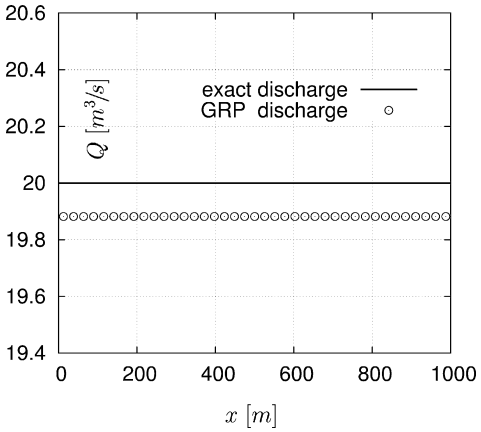

Fig. 15. Channel flow II: flow discharge at large time.

As in the previous example, the smooth initial distribution of flow variables has evolved into a (large time) steady solution that contains a hydraulic jump. The computed discharge value was constant throughout the domain, and in particular across the hydraulic jump, as shown in Fig. 15. The relative discharge deviation of 0.6% results from not imposing the exact inflow boundary condition, but rather specifying the exact inflow as the left-side data for the generalized Riemann problem at the leftmost point. The results indicate that the GRP scheme adheres closely to a conservation laws formulation. Note that in a study by Delis et al. [7], where several finite-difference methods (MUSCL and some implicit TVD schemes) were applied to similar test problems (also due to Macdonald et al. [14]), significant discharge fluctuations were observed near the hydraulic jump.

6. Concluding remarks

The subject of this article is the GRP method for the shallow water equations that govern unsteady flow in long channels of locally rectangular cross-section. This system is quasi-one-dimensional, and includes the effects of smoothly varying width and bed elevation; a shear stress at the channel–fluid interface is accounted for by the Manning friction model. The proposed GRP method is a second-order accurate extension to the classical Godunov-scheme, using at each cell-interface the analytic solution to a generalized Riemann problem (GRP), which is the initial value problem for the full PDE with piecewise-linear data in cells. It treats the geometric terms corresponding to varying width and bed elevation in a novel way. The variable width is fully

included in the upwind second-order differencing of the homogeneous part of the considered system. In particular, no time-splitting or fractional time step technique are required to handle source terms arising from considering the constant-width system as the homogeneous part of the PDE. The bed slope source term is handled by the Surface Gradient Method (SGM) of Zhou et al.[17] which has been incorporated into the GRP framework. It has been shown that the resulting scheme possesses the Z-property (as does the original SGM), meaning that it exactly replicates a state of quiescent flow in a channel of varying bed elevation. Another novel feature of GRP is that the second-order component of the state time-derivative reflects the effect of the full PDE, rather than just its homogeneous part. These features produce accurate high-resolution solutions for quasi-1D problems (including cylindrical symmetry), as demonstrated by an array of channel flow problems.

To test the scheme, five sample problems are considered in detail. They include various combinations of variable width, variable bed elevation and friction modeling of shear stress. The first problem is an unsteady dam break flow in a constant-width flat bed channel, for which an error norm was evaluated (using the exact solution) and compared to errors published for other schemes. The second is an unsteady cylindrical dam break with a flat bed; the GRP solution compares favorably to an accurate numerical one. The third is LeVeque's perturbation test problem with bottom topography, where the GRP solution seems comparable to solutions obtained by other schemes, demonstrating the Z-property of our scheme. The fourth is a steady-state flow in a flat-bed channel of variable width, with boundary conditions that produce a hydraulic jump at large time; it compares quite well to the exact solution. Finally, the fifth example is a steady flow where all features appearing in the governing equations – variable width, bed profile and friction are included. The computed large time results show remarkable agreement with the exact solution, and the constant discharge demonstrates convergence.

Acknowledgements

We are grateful to Professor M. Ben-Artzi of the Institute of Mathematics, the Hebrew University of Jerusalem, for introducing us to mathematical aspects of the shallow water equations. We gratefully acknowledge the warm hospitality and support of Professor Roberts and the Centre for Mathematics and its Applications, at ANU, Canberra, where the bulk of this research was conducted. The support by Dr. C. Zoppou of Geoscience Australia in Canberra is also gratefully acknowledged.

Appendix A. Proof of scheme compliance to Z-property

We claim that the time-integration of the governing equations by the computational procedure presented in Section 4 replicates a state of quiescent flow, where the initial water level $\zeta(x,0) = h(x,0) + Z(x) = \text{constant}$ and the initial velocity $u(x,0) = 0$. Since the scheme is of second-order accuracy, the maintenance of an equilibrium state requires that both first-order and second-order terms vanish. The proof of this claim is two-staged: First, it is shown that the time-derivatives of h, u at cell-boundary points vanish, and hence, by (2.2), the mid-point values $\mathbf{U}^{n+\frac{1}{2}}_{i+\frac{1}{2}}$ are identical to the respective first-order values $\mathbf{U}^{n}_{i+\frac{1}{2}}$. Second, it is shown that the subsequent integration by the finite-difference relation (2.1) leaves a state of hydrostatic equilibrium unchanged.

Clearly, the water-level (ζ) and depth (h) reconstruction procedure according to steps (4.4)–(4.7) replicates the initial flat surface. Hence, the resulting data for the point-centered associated RP's at cell boundaries is continuous, i.e., $u^n_{i+\frac{1}{2},\mathrm{L}} = u^n_{i+\frac{1}{2},\mathrm{R}} = 0$, $h^n_{i+\frac{1}{2},\mathrm{L}} = h^n_{i+\frac{1}{2},\mathrm{R}}$. With this data the solution to associated RP's at cell boundaries (see Section 4.5) is the identity solution ($u^* = 0$, $h^* = h^n_{i+\frac{1}{2},\mathrm{L}} = h^n_{i+\frac{1}{2},\mathrm{R}}$). It follows that the (x,t) trajectories of cell-boundaries points are $\mathrm{d}x/\mathrm{d}t = \mathrm{d}\xi/\mathrm{d}t = 0$ (i.e., in the range of Sectors $v = 3,4$ in Fig. 4). The respective Eulerian time-derivatives of u, h are hence given by (3.33) in terms of the Lagrangian time-derivatives of u^*, h^*, which are in turn given by (3.12). Therefore, in order to prove that the Eulerian time-derivatives at cell boundaries vanish, all we have to show is that in a state of equilibrium the coefficients $d_{\mathrm{L}}, d_{\mathrm{R}}$ appearing in (3.12), vanish.

Consider the shock case, with the coefficient d_{R} given in (3.16). At equilibrium $\eta = 1$ and $u^* = 0$, so that the expression for d_{R} reduces to $d_{\mathrm{R}} = L_h h'_{\mathrm{R}} + (L_S + g)S_0$. In this case $L_S + g = 2g$, $L_h = -2b(0)gh_{\mathrm{R}}$, and since $h'_{\mathrm{R}} = (\partial h/\partial x)_{\mathrm{R}}/(b(0)h_{\mathrm{R}})$ we get

$$d_{\mathrm{R}} = -2g\left[\frac{\partial(h+Z)}{\partial x}\right]_{\mathrm{R}}. \tag{A.1}$$

By virtue of the "one-sided" expressions for the Z-slopes in (4.8) and the h-slopes in (4.9), the derivative in (A.1) vanishes and so does d_{R}.

In the CRW case where the coefficient d_{L} is given by (3.29), we notice that since $u^* = 0$ and $\beta^* = 1$, the expression for d_{L} reduces to $d_{\mathrm{L}} = -\kappa_{\mathrm{L}} b(0)a(1)$. It is thus left to be shown that $a(1) = 0$ in a state of equilibrium. We start out from the expression (3.22) for $a(1)$, which since $u'_{\mathrm{L}} = 0$ and $S_{\mathrm{f}} = 0$, reduces to $a(1) = (c_{\mathrm{L}}/h_{\mathrm{L}})h'_{\mathrm{L}} + (g/h_{\mathrm{L}}^3)^{1/2}Z'(x)/b(0)$. Using the Lagrange-to-Euler relation for the h-derivative as for h'_{R} above, we finally get

$$d_{\mathrm{L}} = -g\left[\frac{\partial(h+Z)}{\partial x}\right]_{\mathrm{L}}. \tag{A.2}$$

As before, the spatial derivative in (A.2) vanishes, and hence d_{L} vanishes.

These results have in fact motivated the "one-sided" expressions (4.8), (4.9) for the slopes of h and Z. Moreover, it also prompted the six-sector division in Fig. 4 where a virtual contact-discontinuity (moving at velocity u^*) is retained.

We now turn to the time-integration of h, hu according to the finite-difference relation (2.1). Since the solution to associated RP's in this case is $u^n_{i+\frac{1}{2}} = 0$, $h^n_{i+\frac{1}{2}} = h^n_{i+\frac{1}{2},\mathrm{L}} = h^n_{i+\frac{1}{2},\mathrm{R}}$, the time-derivative for h in (2.1) clearly vanishes, and the time-derivative for (hu) reduces to

$$\frac{(hu)_i^{n+1} - (hu)_i^n}{\Delta t} = \frac{g}{\Delta x}\left(h^n_{i+\frac{1}{2}} - h^n_{i-\frac{1}{2}}\right)\left[\frac{1}{2}\left(h^n_{i+\frac{1}{2}} + h^n_{i-\frac{1}{2}}\right) - h^n_i\right] = 0, \tag{A.3}$$

where we have used $(S_0)_i = -\Delta Z_i/\Delta x$, and by (4.7) we have in this case $-\Delta Z_i = \Delta h^n_i = (h^n_{i+\frac{1}{2}} - h^n_{i-\frac{1}{2}})$ (since here $\Delta\zeta^n_i = 0$).

References

[1] M. Ben-Artzi, J. Falcovitz, A second-order Godunov-type scheme for compressible fluid dynamics, J. Comput. Phys. 55 (1984) 1–32.
[2] M. Ben-Artzi, J. Falcovitz, An upwind second-order scheme for compressible duct flows, SIAM J. Sci. Statist. Comput. 7 (1986) 744–768.
[3] M. Ben-Artzi, J. Falcovitz, Generalized Riemann Problems in Computational Fluid Dynamics, Cambridge University Press, London, 2003.
[4] A. Bermúdez, M.E. Vázquez, Upwind methods for hyperbolic conservation laws with source terms, Comput. Fluids 23 (1994) 1049–1071.
[5] S.J. Billett, E.F. Toro, On WAF-type schemes for multidimensional hyperbolic conservation laws, J. Comput. Phys. 130 (1997) 1–24.
[6] R. Courant, K.O. Friedrichs, Supersonic Flow and Shock Waves, Springer, New York, 1976.
[7] A.I. Delis, C.P. Skeels, S.C. Ryrie, Implicit high-resolution methods for modelling one-dimensional open channel flow, J. Hydraul. Res. 38 (2000) 338–369.
[8] P. Garcia-Navarro, F. Alcrudo, J.M. Savirón, 1D open channel flow simulation using TVD MacCormack scheme, J. Hydraul. Eng. 118 (1992) 1359–1372.
[9] S.K. Godunov, A difference scheme for the numerical computation of discontinuous solutions to the equations of fluid dynamics, Mat. Sbornik 47 (1959) 271–306.
[10] C.W. Hirt, A.A. Amsden, An arbitrary Lagrangian Eulerian computing method for all flow speeds, J. Comput. Phys. 14 (1974) 227–253.
[11] L.D. Landau, E.M. Lifshitz, Fluid Mechanics, Pergamon Press, 1959.
[12] R.J. LeVeque, Balancing source terms and flux gradients in high-resolution Godunov methods: the quasi-steady wave-propagation algorithm, J. Comput. Phys. 146 (1998) 346–365.
[13] Jiequan Li, Guoxian Chen, The generalized Riemann problem method for the shallow water equations with bottom topography, Int. J. Numer. Methods Eng. 6 (2006) 834–862.
[14] I. MacDonald, M.J. Braines, N.K. Nichols, P.G. Samuels, Analytic benchmark solution of open-channel flows, J. Hydraul. Eng. 123 (1997) 1041–1045.
[15] B. van Leer, Towards the ultimate conservative difference scheme V, J. Comput. Phys. 32 (1979) 101–136.

[16] M.E. Vázquez-Cendón, Improved treatment of source terms in upwind schemes for shallow water equations in channels with irregular geometry, J. Comput. Phys. 148 (1999) 497–526.
[17] J.G. Zhou, G.M. Causon, C.G. Mingham, D.M. Ingram, The surface gradient method for the treatment of source terms in the shallow-water equations, J. Comput. Phys. 168 (2001) 1–25.
[18] C. Zoppou, S. Roberts, Explicit schemes for dam-break simulations, J. Hydraul. Eng. 129 (2003) 11–34.
[19] C. Zoppou, S. Roberts, Numerical solution of the two-dimensional unsteady dam-break, Appl. Math. Modell. 24 (2000) 457–475.